AIAA JOURNAL
Vol. 44, No. 5, May 2006

Jet Screech Noise Computation

Ching Y. Loh* and Lennart S. Hultgren†
NASA John H. Glenn Research Center at Lewis Field, Cleveland, Ohio 44135

The near-field screech-tone noise of a typical underexpanded circular jet issuing from a sonic nozzle is simulated numerically. The self-sustained feedback loop is automatically established in the simulation. The computed shock-cell structure, acoustic wave length, screech-tone frequencies, and sound pressure levels in the near field are in good agreement with existing experimental results.

I. Introduction

JET noise is an important and still challenging topic in aeroacoustics. Many of its aspects are of primary practical importance, and the associated complicated physical phenomena are the topic of many experimental and theoretical investigations. In Refs. 1–4, a comprehensive discussion and further references are provided. Under/overexpanded supersonic jets emit mixing noise, broadband shock-associated noise, as well as screech tones under certain conditions. The mixing noise is directly associated with large-scale structures, or instability waves, in the jet shear layer, and the broadband shock-associated noise is caused by the interaction of these waves with the shock-cell structure in the jet core. The screech tones arise due to a feedback loop involving the large-scale structures developing in the jet shear layer, their interaction with the jet-core shock-cell structure producing upstream propagating acoustic waves, and regeneration of the large-scale structures at, or in the vicinity of, the nozzle lip. This feedback loop leading to screech tones is sensitive to small changes in the system conditions, and the understanding of the phenomena to date is based mostly on experimental observations.[5–9] Screech is of particular interest not only because of general noise-reduction concerns, but also because of potentially destructive structural interaction leading to sonic fatigue.

Reliable numerical simulation of jet screech noise, that is, near-field noise computation in the presence of shock cells in the jet core, has only quite recently become feasible. It is a challenge in that the numerical scheme must 1) handle shock waves, 2) resolve acoustic waves with low dispersion and dissipation errors, 3) resolve the instability waves in the jet shear layer and their interaction with the core shock-cell structure, and 4) have an effective nonreflecting boundary condition. Successful direct computation of screech for circular jets have been carried out by Shen and Tam[10–12] using the dispersion relation preserving (DRP) scheme and by Loh et al.,[13] Loh and Hultgren,[14] Jorgenson and Loh,[15] and Loh et al.[16] using a Navier–Stokes solver based on the space–time conservation element and solution element (CE/SE) method.[17,18] In their three-dimensional computation, Shen and Tam[12] adopted a spectral method in the azimuthal direction, and by using only a limited number of spectral functions achieved substantial savings of computer memory and CPU time, without deterioration of accuracy. Other recent computational work includes Refs. 19 and 20.

In general, the CE/SE method systematically solves a set of discretized space–time integral equations derived directly from the physical conservation laws and naturally captures shocks and other discontinuities in the flow. The method may be categorized as a finite volume method, where the conservation element (CE) is equivalent to a finite control volume (cell) and the solution element (SE) can be understood as the space–time cell interface. The scheme is second-order accurate in both space and time, and the space–time surface fluxes are carefully calculated. Despite its formal second-order accuracy, it possesses low dispersion error and low dissipation. Multidimensional nonreflecting boundary conditions (NRBCs), based on plane-wave propagation principles,[21] are easily implemented. In principle, these NRBCs are equivalent to using characteristics but are simpler to apply. With these NRBCs, a small near-field computational domain can be used. The CE/SE procedure is also easily adapted to complicated geometries using unstructured grids. The method is robust enough to cover a wide spectrum of compressible flow, from weak linear acoustic waves to shocks; hence, it is an appropriate tool for the present jet screech computation. Details of the method are described in Refs. 13, 17, and 22.

II. Axisymmetric Jet Screech Problem

Figure 1a shows the geometry of the convergent nozzle in Panda's experiment.[9] The flow is choked, that is, Mach number $M_e = 1$, at the nozzle exit. The operating condition of the jet is fully described by additionally specifying the plenum (reservoir) to ambient pressure and temperature ratios, respectively. The pressure ratio is commonly expressed in terms of the jet Mach number M_j, which would be the exit Mach number of the corresponding perfectly expanded jet. For the cold-flow situation (unity temperature ratio) considered in Ref. 9, the dominating screech-tone mode is axisymmetric for $M_j \leq 1.19$. Hence, the numerical simulation can employ an axisymmetric CE/SE Navier–Stokes solver for these operational conditions. Furthermore, the attention is focused here on the near field of the nozzle because this is the noise source region. The diameter D of the jet nozzle is chosen as the length scale; the density ρ_∞, speed of sound a_∞, and temperature T_∞ in the ambient flow are taken as scales for the dependent variables; all other scales are constructed from these. The computational domain (Fig. 1b), spans between $-8.3 \leq x \leq 6$ and $0 \leq r \leq 11.7$, with x and r being the nondimensional streamwise and radial coordinates. The flow inside the nozzle is not computed, rather the steady flow conditions are prescribed at the nozzle exit, which is located at $x = 0$. This inflow plane is recessed by two cells to not restrict numerically or influence the feedback loop. The numerical scheme[13,14] utilizes a triangulated grid of about 230,000 cells. The triangular cells are generated by dividing rectanglelike quadrilaterals. In the region deemed crucial for the acoustic-feedback path, that is, $0 \leq x \leq 3.2$ and $0 \leq r \leq 1$, the resulting streamwise and spanwise grid resolution is about 0.03 and 0.0125, respectively. Outside of this region, the grid is gently stretched, in both directions, leading to an increase in the cell dimensions by about a factor of three near the computational boundary. An advantage of using quadrilaterals is good control of mesh size and and quality. Nonreflecting boundary conditions are applied to the upper and outflow boundaries, and a symmetry condition is applied at the center axis. The last 10 streamwise cells are exponentially stretched and serve as a buffer, or sponge, zone essentially to eliminate any small remaining numerical reflection from the downstream outflow boundary.

Received 14 August 2003; revision received 12 August 2005; accepted for publication 17 August 2005.

*Senior Research Scientist, Taitech, Inc. Member AIAA.
†Senior Aerospace Research Engineer, Propulsion Systems Division. Associate Fellow AIAA.

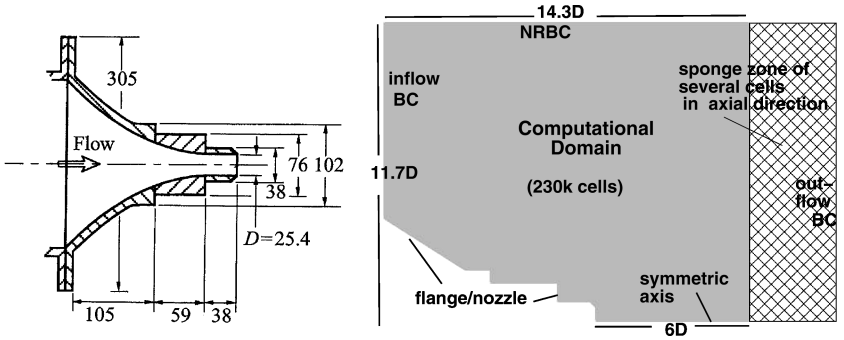

Fig. 1 Near-field geometry: a) geometry of the convergent nozzle and flange in Panda's experiment[9] (dimensions in millimeters) and b) computational domain.

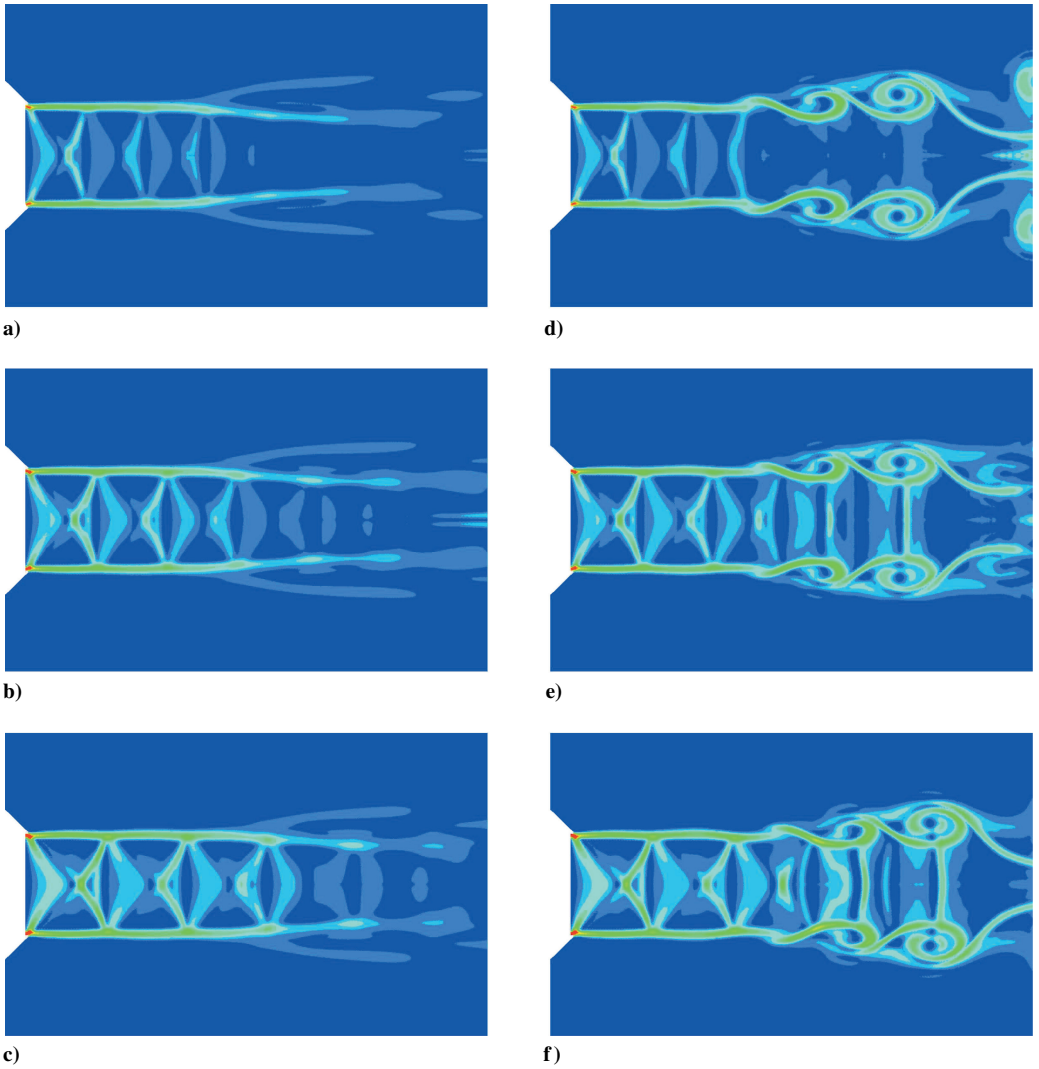

Fig. 2 Numerical schlieren results (density gradient modulus) at $t = 410{,}000$ steps results: a) time averaged, $M_j = 1.11$; b) time averaged, $M_j = 1.15$; c) time averaged, $M_j = 1.19$; d) instantaneous, $M_j = 1.11$; e) instantaneous, $M_j = 1.15$; and f) instantaneous, $M_j = 1.19$. Same M_j in rows; time-averaged and instantaneous results in left and right columns.

Initially, the entire flowfield is at rest and at ambient conditions, that is, when nondimensional variables are used,

$$\rho_0 = 1, \qquad p_0 = 1/\gamma, \qquad T_0 = 1, \qquad u_0 = 0, \qquad v_0 = 0$$

where ρ, p, T, u, v, and γ are the density, static pressure, temperature, streamwise velocity component, radial velocity component, and constant specific heat ratio, respectively. The jet flow is then impulsively started. At the inlet boundary, the conservative flow variables [Appendix Eq. (A2)] and their spatial derivatives are specified to be those of the ambient flow, except at the nozzle exit, where an elevated pressure is imposed, that is, the jet is underexpanded, as in the physical experiments. When the ideal gas isentropic relations are used, it follows that the nondimensional flow variables at the nozzle exit, with $M_e = 1$, are given by

$$\rho_e = \frac{\gamma p_e}{T_e}, \qquad p_e = \frac{1}{\gamma}\left[\frac{2 + (\gamma - 1)M_j^2}{\gamma + 1}\right]^{\gamma/(\gamma-1)}$$

$$T_e = \frac{2T_r}{\gamma + 1}, \qquad u_e = T_e^{\frac{1}{2}}, \qquad v_e = 0$$

where T_r is the reservoir (plenum) temperature. We will also follow the experimental cold-flow condition, where the reservoir temperature equals the ambient one, that is, $T_r = 1$. The Reynolds number $Re = Da_\infty/\nu = 570{,}000$, where ν is the kinematic viscosity at the ambient conditions. The weighted average a–ε CE/SE scheme[22] is used with the weighting parameter $\alpha = 1$ and $\varepsilon = 0.5$ in the present computation.

III. Numerical Results and Comparison to Experiments

In this section, various computed results are compared to the experimental findings of Panda.[9] Figure 2 shows numerical schlieren (density gradient modulus) contours, well after the startup transients have passed out of the computational domain for the cases of $M_j = 1.11$, 1.15, and 1.19, top, middle, and bottom rows, respectively. The left and right columns show time-averaged and instantaneous results, respectively. Figure 2 clearly shows the shock-cell structure, as well as its deformation and destruction by the spatially growing large-scale structures in the jet shear layer. The shock-cell spacing of $0.8D$ at $M_j = 1.19$ agrees well with the experimental result of Ref. 9, Fig. 5b, reproduced here as Fig. 3.

Figure 4 shows numerical time-averaged density results for the case of $M_j = 1.19$. Radial mean density profiles for 16 streamwise stations, $x = 0, 0.3, 0.6, \ldots, 4.5$, are shown in Fig. 4a, and Fig. 4b shows mean density contours in the x–r plane. The profiles show the streamwise evolution of the jet shear layer. Inside the potential core, the presence of the shock cells causes significant changes in the profiles compared to what would have been the case for a perfectly expanded jet. Just as observed in experiments,[23] the jet spreading is initially relatively slow, but it shows a significant increase after about $x = 2$. The corresponding numerical time-averaged results for the streamwise velocity is shown in Fig. 5. Figure 5a shows

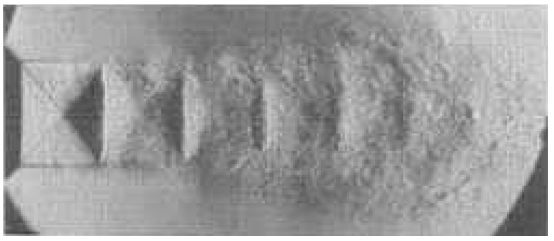

Fig. 3 Shock-cell structure for $M_j = 1.19$, experimental schlieren picture (Ref. 9, Fig. 5b).

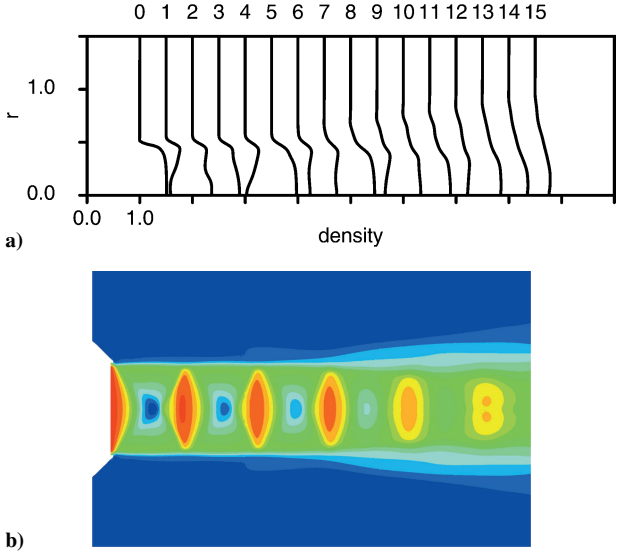

Fig. 4 Numerical mean density results for $M_j = 1.19$: a) radial density profiles for 16 streamwise stations ($x = 0, 0.3, 0.6, \ldots, 4.5$) labeled 0–15 and b) density contours.

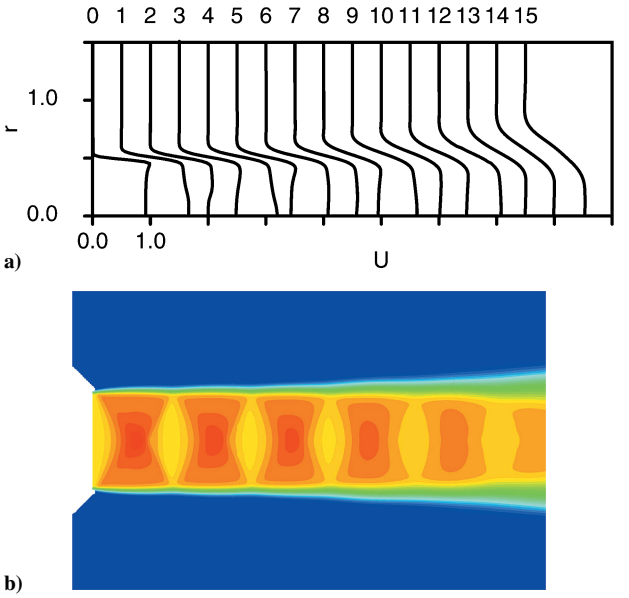

Fig. 5 Numerical mean streamwise velocity results for $M_j = 1.19$: a) radial streamwise velocity profiles for 16 streamwise stations ($x = 0, 0.3, 0.6, \ldots, 4.5$) labeled 0–15 and b) streamwise velocity contours.

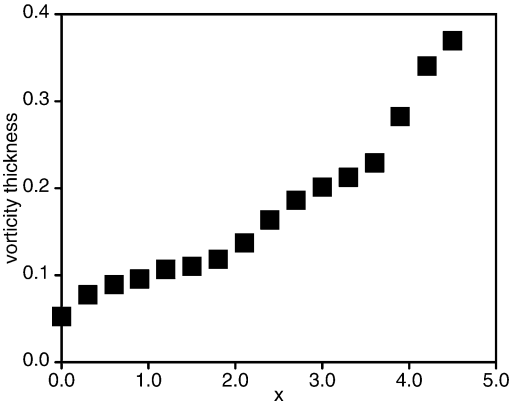

Fig. 6 Numerical mean vorticity thickness for $M_j = 1.19$.

radial mean streamwise velocity profiles for the same 16 streamwise stations, and mean streamwise velocity contours in the x–r plane are shown in Fig. 5b. The streamwise velocity profiles are also significantly altered inside the potential core due to the presence of the shock cells. Figure 5 also shows a change in the spreading of the jet around $x = 2$. Figure 6 shows the streamwise evolution of the shear-layer vorticity thickness. The vorticity thickness is customarily defined as $\delta_v = \Delta U/|(\mathrm{d}U/\mathrm{d}r)_{\max}|$, where ΔU is the velocity change across the (circular) shear layer. Because of the overshoot visible in the radial profiles at several streamwise stations, the vorticity thickness presented in Fig. 6 was computed as $\min(U_j, U_{\max})/|(\mathrm{d}U/\mathrm{d}r)_{\max}|$ from the time-averaged radial streamwise velocity profiles, where U_j is the (theoretical) fully expanded jet velocity (1.05 for $M_j = 1.19$). The increase in the shear layer spreading at about $x = 2$ is evident in this figure.

Figure 7 shows instantaneous numerical isobars well after the startup transients have passed out of the computational domain for the cases of $M_j = 1.11$, 1.15, and 1.19. The contours shown are for the fluctuating part of the pressure, that is, the time-averaged pressure at each spatial location has been subtracted. Distinct screech waves are observed to emit from the third to the fifth shock-cell and are reflected at the flange/nozzle body. The screech wavelength ($1.6D$) at $M_j = 1.19$ agrees well with the experiment.[9] Spectral analysis yields a computed screech frequency of 8513 Hz, which agrees well with the experimental value of 8525 Hz.

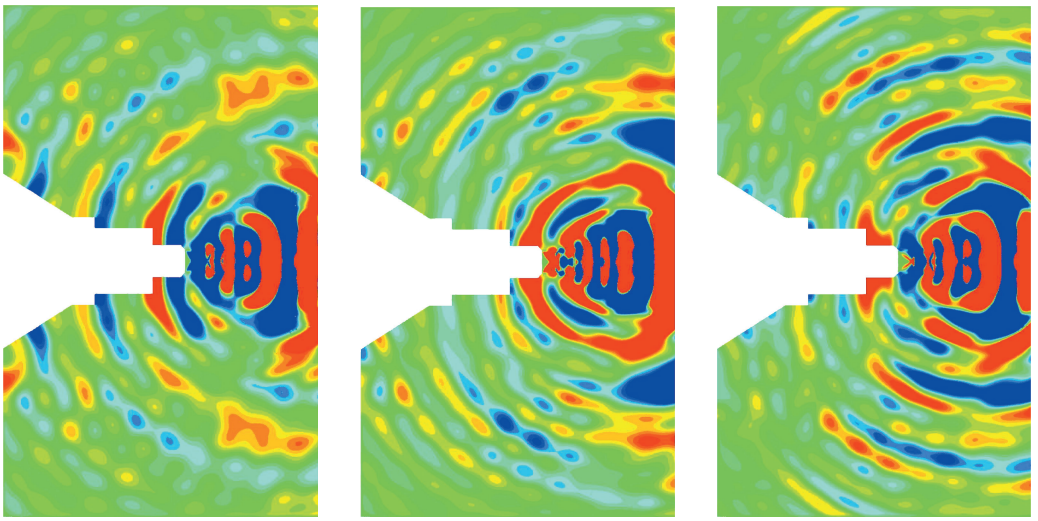

a) b) c)

Fig. 7 Instantaneous differential isobars, at $t = 410{,}000$ steps, showing screech waves: a) $M_j = 1.11$, b) $M_j = 1.15$, and c) $M_j = 1.19$.

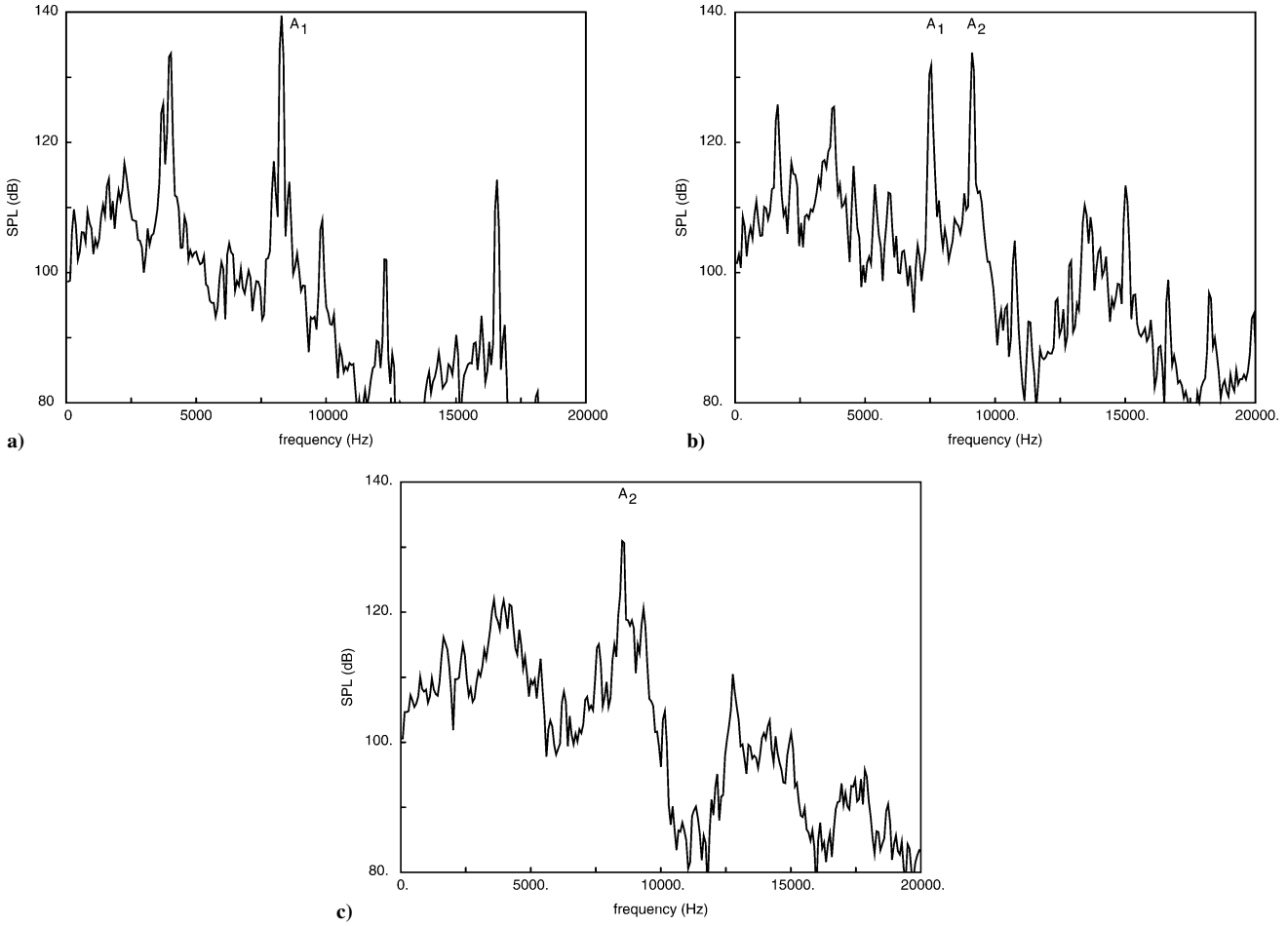

Fig. 8 Narrowband SPL distribution at nozzle exit ($x = 0$ and $r = 0.6$), 75-Hz digital binwidth: a) $M_j = 1.11$, A_1 mode 8289 Hz; b) $M_j = 1.15$, A_1 mode 7542 Hz, and A_2 mode 9110 Hz; and c) $M_j = 1.19$, A_2 mode 8513 Hz.

The spectral results are obtained by saving time-series data at various locations in the flowfield. This starts after 80,000 time steps to ensure that all startup transients have passed out of the computational domain. The instantaneous pressure at each selected location is then saved every 20 steps of the subsequent 330,000 steps of the simulation. The time histories are then each divided up in overlapping segments and analyzed using discrete Fourier transform techniques to obtain the power spectral density (PSD), using standard techniques, for example, Ref. 24. The pressure PSD is then simply renormalized to yield the narrowband sound pressure level (SPL) distribution.

Figure 8 shows computed SPL distributions (narrowband) at the nozzle exit lip wall ($x = 0$ and $r = 0.6$) for $M_j = 1.11, 1.15$, and 1.19. The SPL distributions show distinct spikes corresponding to the A_1 and A_2 axisymmetric screech-tone modes observed in Panda's[9] experiment. For $M_j = 1.15$, both the A_1 and A_2 modes are dominating

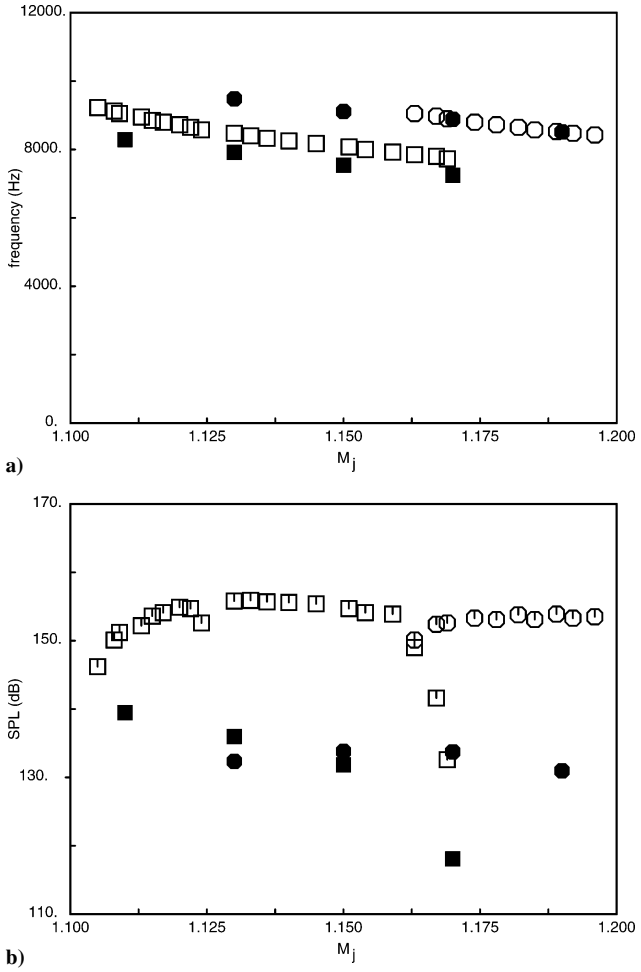

Fig. 9 Comparison of computed and experimental[9] results: a) screech-tone frequency vs M_j and b) screech-tone SPL at nozzle exit ($x = 0, r = 0.6$) vs M_j: □ and ■, A_1 mode; ○ and ●, A_2 mode; filled symbols, numerical simulation and open symbols, Panda's experiment.

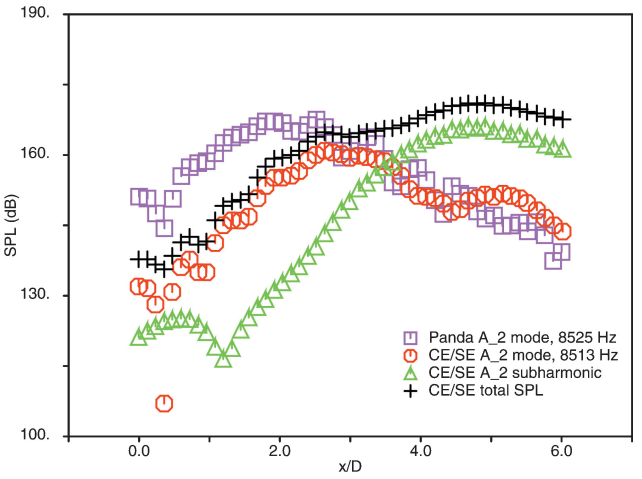

Fig. 10 Comparison of computed and experimental[9] SPL along the shear layer edge, $M_j = 1.19$.

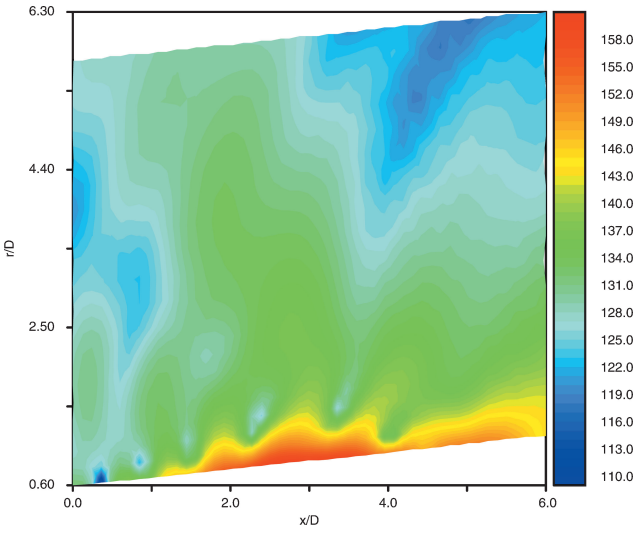

Fig. 11 Computed A_2-mode SPL levels for Panda's experiment,[9] $M_j = 1.19$.

features, whereas only the A_1 mode is dominating at $M_j = 1.11$ and only the A_2 mode is dominating at $M_j = 1.19$. Note that in our earlier work,[13] where a much simplified description of the nozzle external geometry was used, the A_1-mode screech tone (not observed in Ref. 9) was also prominent at the latter jet Mach number. This illustrates the sensitivity of the screech phenomenon to geometry changes. Figure 9 shows a comparison of the current numerical with Panda's experimental results[9] for the A_1 and A_2 screech-tone frequencies and SPL at the nozzle lip, both as functions of the jet Mach number. The screech-tone frequencies are well predicted, whereas the numerical SPL values are somewhat low.

As is well known, the feedback loop leading to screech is very sensitive to small changes in system conditions and can even vary between experiments for seemingly the same conditions. The feedback loop is closed in the very vicinity of the nozzle lip where the shear layers are very thin and are rapidly adjusting from having been wall bounded inside the nozzle. Any imperfections in the simulation are most likely to affect the results in this region. Numerical dissipation, although small enough to not affect substantially the results in other flow regions, could be the reason that the SPL level is too low in the vicinity of the nozzle lip. Note, that, as will be seen later, the SPL levels are not uniformly underpredicted in other regions of the flow.

The SPL along an inclined line at the outer edge of the shear layer is shown in Fig. 10 for $M_j = 1.19$. Figure 10 shows Panda's[9] data for the A_2 axisymmetric screech mode, the corresponding result from the simulation, as well as the computed total SPL and subharmonic of the A_2 mode. Even though the A_2 SPL level in the vicinity of the nozzle lip is too low, its early streamwise growth rate is, however, well predicted, indicating that the jet shear layer is in general well resolved. Nonlinearity in the shear layer limits the amplitude that can be obtained, and once the SPL level catches up, the agreement is very good. In particular the SPL level in the streamwise region where the backward radiating acoustic waves are generated is well predicted. The strong subharmonic that appears farther downstream is due to (axisymmetric) vortex pairing in the shear layer, and as a consequence, a second streamwise peak at the A_2 frequency occurs due to nonlinear effects. These nonlinear effects are also responsible for the (second) distinct increase in the computed shear-layer spreading rate that can be seen to occur at about $x = 4$ in Fig.6. However, three-dimensional effects are most likely to have come into play in the experiment at these streamwise locations leading to suppression of the subharmonic. The subgrid-scale eddy-viscosity model used in the present computation [Appendix, Eq. (A3)] does reduce the subharmonic somewhat, but cannot suppress it because the model does not describe the effects of large-scale three-dimensional motions that ultimately become important at these streamwise locations.

Figure 11 shows computed SPL contours for the A_2 mode. As in the experiment,[9] a standing wave structure can be observed along the edge of the jet shear layer. As explained by Panda,[9] the standing wave formation is due to combination of the downstream-propagating hydrodynamic and upstream-propagating acoustic fluctuations, both integral parts of the screech feedback loop. The results are in general agreement with the experimental ones except, as pointed out earlier, that the computed SPL levels are too low in the vicinity of the nozzle

lip and the existence of a second, or extended, region of elevated values farther downstream ($x/D > 4$).

IV. Conclusions

In this paper, screech-tone noise analysis of an underexpanded supersonic axisymmetric jet was carried out using a finite volume numerical scheme. Many hydrodynamic and acoustic aspects of the computed results are in good agreement with experimental findings,[8,9] including the variation of screech frequency with Mach number for the axisymmetric A_1 and A_2 modes. Because no forcing was applied in these simulations, the numerical results clearly indicate the presence of a self-sustained oscillation. Large-eddy simulation modeling was used to better capture the jet spreading farther downstream, that is, after the initial shear-layer rollup, but is not believed to be a critical element for the screech feedback loop. Note that screech is essentially an inviscid phenomenon. It is concluded that the simulation shows a reasonably good agreement with experimental data in the streamwise region where the flow is expected to be predominantly axisymmetric and, hence, that jet screech is successfully simulated using the present scheme.

The advantages of the present scheme were confirmed in the simulation. The implementation did not require any special treatment or parameter selections to capture both the shock-cell structure or the acoustics. The robust finite volume NRBC in combination with buffer zones virtually eliminates numerical reflections and allows for an effective near-field computation. The use of an unstructured grid also offers flexibility for dealing with more complicated geometries.

Appendix: Governing Equations

The axisymmetric Navier–Stokes equations can be written in the following vector conservation form:

$$\boldsymbol{U}_t + \boldsymbol{F}_x + \boldsymbol{G}_r = \boldsymbol{Q} \tag{A1}$$

where $x, r \geq 0$, and t are the streamwise and radial coordinates and time, respectively. The four components of the conservative flow variable vector $\boldsymbol{U}$ are given by

$$U_1 = \rho, \qquad U_2 = \rho u, \qquad U_3 = \rho v$$

$$U_4 = p/(\gamma - 1) + \rho(u^2 + v^2)/2 \tag{A2}$$

The components of the flux vectors $\boldsymbol{F}$ and $\boldsymbol{G}$ are given by

$$F_1 = U_2$$

$$F_2 = (\gamma - 1)U_4 + \frac{\left[(3-\gamma)U_2^2 - (\gamma-1)U_3^2\right]}{2U_1} - \mu\left(2u_x - \frac{2}{3}\Delta\right)$$

$$F_3 = \frac{U_2 U_3}{U_1} - \mu(u_r + v_x)$$

$$F_4 = \frac{\gamma U_2 U_4}{U_1} - (\gamma - 1)U_2\frac{\left[U_2^2 + U_3^2\right]}{2U_1^2} - \mu\left[2uu_x + v(u_r + v_x) - \frac{2}{3}u\Delta + \frac{\gamma}{Pr}\frac{\partial}{\partial r}\left(\frac{U_4}{U_1} - \frac{u^2+v^2}{2}\right)\right]$$

$$G_1 = U_3, \qquad G_2 = \frac{U_2 U_3}{U_1} - \mu(u_r + v_x)$$

$$G_3 = (\gamma - 1)U_4 + \frac{\left[(3-\gamma)U_3^2 - (\gamma-1)U_2^2\right]}{2U_1} - \mu\left(2v_r - \frac{2}{3}\Delta\right)$$

$$G_4 = \frac{\gamma U_3 U_4}{U_1} - (\gamma - 1)U_3\frac{\left[U_2^2 + U_3^2\right]}{2U_1^2} - \mu\left[2vv_r + u(u_r + v_x) - \frac{2}{3}v\Delta + \frac{\gamma}{Pr}\frac{\partial}{\partial r}\left(\frac{U_4}{U_1} - \frac{u^2+v^2}{2}\right)\right]$$

where u_x, u_r, v_x, and v_r are the spatial derivatives of the streamwise and radial velocity components, which can be written in terms of the conservative variables U_1, U_2, U_3 and U_4, with Pr ($=0.72$) being the Prandtl number, $\mu = 1/Re$ the nondimensional viscosity, and the velocity divergence

$$\Delta = u_x + v_r + v/r$$

The four components of the source term Q are given by

$$Q_1 = -U_3/r, \qquad Q_2 = -U_2U_3/U_1r$$

$$Q_3 = -U_3^2/U_1r, \qquad Q_4 = -G_4(\mu = 0)/r$$

The preceding nondimensional equations would form the basis for a direct numerical simulation. Currently, this is not fully feasible for the high-Reynolds-number flows of interest here. The present computations are of the large-eddy-simulation (LES) type,[25] where scales smaller than the grid resolution are modeled. In this case, the preceding equations are considered the filtered ones governing the resolved scales, where ρ and p are to be interpreted as simply averaged over the subgrid scales and the other dependent variables are to be interpreted as Favré, that is, density-weighted, averages. The simplest model for the effects of the unresolved scales on the motion is obtained by using a Boussinesq eddy-diffusivity assumption for the subgrid shear stresses and heat flux coupled by Smargorinsky's model for the eddy viscosity (for example, see Ref. 26), that is, μ is replaced by

$$\mu = 1/Re + (C_s\delta)^2(S_{ij}S_{ij})^{\frac{1}{2}} \tag{A3}$$

where $S_{ij} = \frac{1}{2}(\partial u_i/\partial x_j + \partial u_j/\partial x_i)$ is the rate-of-deformation tensor, $\delta = (\delta x \delta r)^{1/2}$ is a local measure of the grid size, and C_s is a (nondimensional) constant. Note that the simplifying assumption that the subgrid-scale (SGS) Prandtl number equals the laminar one is also made here; if it is not, then the G_4 component needs to be slightly modified.

Panda et al.[27] investigated the initial status of the shear layer at the nozzle exit using a molecular Rayleigh scattering technique for a range of Mach numbers that spans the current one of interest and found it to be nominally laminar. This means that the small-scale turbulence that needs to be modeled is mainly produced as the jet shear layer rolls up; hence, it is limited to a certain region of the spatial computational domain. Consequently, in the present work, C_s is essentially set to zero for $r > 1.5$ or $x < 3$ and is linearly ramped up for $3 < x < 5$ to the value $C_s = 0.1$ (Ref. 25), which is then used for $r < 1.5$ and $x > 5$.

When x, r, and t are considered as coordinates of a three-dimensional Euclidean space E_3, and Gauss's divergence theorem is used, it follows that Eq. (A1) is equivalent to the following integral conservation law:

$$\oint_{S(V)} \boldsymbol{H}^{(m)} \cdot \mathrm{d}\boldsymbol{S} = \int_V Q_m \,\mathrm{d}V, \qquad m = 1, 2, 3, 4 \tag{A4}$$

where $S(V)$ is the surface around a volume V in E_3 and $\boldsymbol{H}^{(m)} = (F_m, G_m, U_m)$. These equations are discretized and solved using the $a - \varepsilon$ weighted-average CE/SE scheme with $\alpha = 1$ and $\varepsilon = 0.5$; see Refs. 13, 14, and 22 for further details. Note that in Ref. 28 it was pointed out that applying flux limiters to finite volume methods, even in the absence of any explicit LES assumptions, effectively leads to LES schemes with minimal implicit SGS models. In Ref. 29, it was demonstrated through error analysis of a particular scheme that the flux-limiters (essentially low-pass frequency filters) built into the algorithm produce additional terms in the equivalent differential forms of the momentum and energy equations that can be interpreted as the SGS stress tensor and flux, respectively. Hence, there is an additional implicit SGS model inherent in the particular CE/SE scheme used, in addition to the explicit assumption in Eq. (A3).

The computational domain was decomposed into 10 subdomains using the METIS mesh partitioning code[29] freely available from the University of Minnesota. The CE/SE solver implemented message

passing interface (MPI) calls to exchange pertinent data between neighboring subdomains. (Information about MPI can be obtained from URL: http://www-unix.mcs.anl.gov/mpi.) The parallel computations were carried out on the CW-7 Linux PentiumIII cluster at NASA John H. Glenn Research Center.

Acknowledgments

This work received support from the Supersonic Propulsion Technology and Quiet Aircraft Technology Project Offices of NASA John H. Glenn Research Center at Lewis Field. The authors thank J. Panda for fruitful discussions about the jet screech phenomena and for kindly providing his detailed experimental data.

References

[1]Seiner, J. M., "Advances in High Speed Jet Aeroacoustics," AIAA Paper 84-2275, Oct. 1984.

[2]Tam, C. K. W., "Jet Noise Generated by Large Scale Coherent Motion," *Aeroacoustics of Flight Vehicles: Theory and Practice. Volume 1: Noise Sources*, edited by H. H. Hubbard, NASA RP-1258, 1991, pp. 311–390.

[3]Tam, C. K .W., "Supersonic Jet Noise," *Annual Review of Fluid Mechanics*, Vol. 27, 1995, pp. 17–43.

[4]Raman, G., "Advancces in Understanding Supersonic Jet Screech: Review and Perspective," *Progress in Aerospace Sciences*, Vol. 34, Jan. 1998, pp. 45–106.

[5]Ponton, M. K., and Seiner, J. M., "The Effects of Nozzle Exit Lip Thickness on Plume Resonance," *Journal of Sound and Vibrations*, Vol. 154, No. 3, 1992, pp. 531–549.

[6]Ponton, M. K., Seiner, J. M., and Brown, M. C., "Near Field Pressure Fluctuations in the Exit Plane of a Choked Axisymmetric Nozzle," NASA TM 113137, Nov. 1997.

[7]Panda, J., Raman, G., and Zaman, K. B. M. Q., "Underexpanded Screeching Jets from Circular, Rectangular and Elliptic Nozzles," AIAA Paper 97-1623, May 1997.

[8]Panda, J., "Shock Oscillation in Underexpanded Screeching Jets," *Journal of Fluid Mechanics*, Vol. 363, 1998, pp. 173–198.

[9]Panda, J., "An Experimental Investigation of Screech Noise Generation," *Journal of Fluid Mechanics*, Vol. 378, 1999, pp. 71–96.

[10]Shen, H., and Tam, C. K. W., "Numerical Simulation of the Generation of Axisymmetric Mode Jet Screech Tones," *AIAA Journal*, Vol. 36, No. 10, 1998, pp. 1801–1807.

[11]Shen, H., and Tam, C. K. W., "Effects of Jet Temperature and Nozzle-Lip Thickness on Screech Tones," *AIAA Journal*, Vol. 38, No. 5, 2000, pp. 762–767.

[12]Shen, H., and Tam, C. K. W., "Three-Dimensional Numerical Simulation of the Jet Screech Phenomenon," *AIAA Journal*, Vol. 40, No. 1, 2002, pp. 33–41.

[13]Loh, C. Y., Hultgren, L. S., and Jorgenson, P. C. E., "Near Field Screech Noise Computation for an Underexpanded Jet by the CE/SE Method," AIAA Paper 2001-2252, May 2001.

[14]Loh, C. Y., and Hultgren, L. S., "Computing Jet Screech—A Complex Aeroacoustic Feedback System," NASA TM 2002-211807, Aug. 2002.

[15]Jorgenson, P. C. E., and Loh, C. Y., "Computing Axisymmetric Jet Screech Tones Using Unstructured Grids," AIAA Paper 2002-3889, July 2002.

[16]Loh, C. Y., Himansu, A., and Hultgren, L. S., "A 3-D CE/SE Navier–Stokes Solver with Unstructured Hexahedral Grid for Computation of Nearfield Jet Screech Noise," AIAA Paper 2003-3207, May 2003.

[17]Chang, S.-C., Wang, X.-Y., and Chow, C.-Y., "The Space–Time Conservation Element and Solution Element Method—A New High Resolution and Genuinely Multidimensional Paradigm for Solving Conservation Laws," *Journal of Computational Physics*, Vol. 156, No. 1, 1999, pp. 89–136.

[18]Loh, C. Y., Hultgren, L. S., and Chang, S.-C., "Computing Waves in Compressible Flow Using the Space-Time Conservation Element Solution Element Method," *AIAA Journal*, Vol. 39, No. 5, 2001, pp. 794–801.

[19]Imamoglu, B., and Balakumar, P., "Computation of Shock Induced Noise in Imperfectly Expanded Supersonic Jets," AIAA Paper 2002-2527, June 2002.

[20]Al-Quadi, I. M. A., and Scott, J. N., "High-Order Three-Dimensional Numerical Simulation of a Supersonic Rectangular Jet," AIAA Paper 2003-3238, May 2003.

[21]Loh, C. Y., "On the Nonreflecting Boundary Condition for Hyperbolic Conservation Laws," AIAA Paper 2003-3975, June 2003.

[22]Wang, X.-Y., and Chang, S.-C., " A 2-D Non-Splitting Unstructured Triangular Mesh Euler Solver Based on the Space-Time Conservation Element and Solution Element Method," *Computational Fluid Dynamics Journal*, Vol. 8, No. 2, 1999, pp. 309–325.

[23]Panda, J., and Seasholtz, R. G., "Measurements of Shock Structure and Shock–Vortex Interaction in Underexpanded Jets Using Rayleigh Scattering," *Physics of Fluids*, Vol. 11, No. 12, 1999, pp. 3761–3777.

[24]Press, W. H., Teukolsky, S. A., Vetterling, W. T., and Flannery, B. P., *Numerical Recipes in C: The Art of Scientific Computing*, 2nd ed., Cambridge Univ. Press, New York, 1992, pp. 496–608.

[25]Lesieur, M., and Métais, O., "New Trends in Large-Eddy Simulation of Turbulence," *Annual Review of Fluid Mechanics*, Vol. 28, 1996, pp. 45–82.

[26]Bogey, C., Bailly, C., and Juvé, D., "Noise Investigation of a High Subsonic, Moderate Reynolds Number Jet Using a Compressible Large Eddy Simulation," *Theoretical and Computational Fluid Dynamics*, Vol. 16, No. 4, 2003, pp. 273–297.

[27]Panda, J., Zaman, K. B. M. Q., and Seasholtz, R. G., "Measurements of Initial Conditions at Nozzle Exit of High Speed Jets," AIAA Paper 2001-2143, May 2001.

[28]Fureby, C., and Grinstein, F. F., "Monotonically Integrated Large Eddy Simulation of Free Shear Flows," *AIAA Journal*, Vol. 37, No. 5, 1999, pp. 544–556.

[29]Karypis, G., and Kumar, V., "Multilevel k-Way Partitioning Scheme for Irregular Graphs," *Journal of Parallel and Distributed Computing*, Vol. 48, No. 1, 1998, pp. 96–129.

A. Karagozian
Associate Editor